Electronic Supplementary Information for

Prediction of superconductivity in a series of tetragonal transition metal dichalcogenides

Jiale Liu, Huidong Wang, Xiaojun Shi, and Xiaoming Zhang*

College of Physics and Optoelectronic Engineering, Ocean University of China, Qingdao, Shandong 266100, China

*Correspondence to: zxm@ouc.edu.cn

Content

Section 1. Details of first-principles calculations on *d*Lieb-MS_2 monolayer……2

Section 2. The magnetic property of *d*Lieb-MnS_2 monolayer……8

Section 3. Details of estimating the superconductivity of *d*Lieb-MS_2 monolayer…....11

Section 4. The feasibility of exfoliating *d*Lieb-MS_2 monolayer……...13

References……...18

Section 1. Details of first-principles calculations on *d*Lieb-MS_2 monolayer

We employed the Quantum ESPRESSO (QE) package [1] to calculate the phonon spectra of *d*Lieb-MS_2 monolayers within the framework of density functional theory (DFT) [2, 3] and density functional perturbation theory (DFPT) [4]. The generalized gradient approximation (GGA) in the functional type of Perdew-Burke-Ernzerh (PBE) [5] was employed for the PAW pseudopotential [6] and the energy cutoff was set to 100 Ry. The crystal structures of *d*Lieb-MS_2 monolayers were fully optimized with a convergence threshold of 10^{-4} for energy and 10^{-3} for force under the **k**-point sampling of 20×20×1 in Brillouin zone. The population of electrons was determined by the gaussian smearing with the smearing type of Methfessel-Paxton first-order spreading and the smearing width of 0.01 Ry. The dynamic matrix and phonon frequency of optimized *d*Lieb-MS_2 were computed on a 10×10×1 **q**-point sampling in Brillouin zone.

The Vienna *Ab initio* Simulation Package (VASP) [7] was employed to calculate the elastic constants and electronic properties of *d*Lieb-MS_2 monolayers based on the DFT [2, 3], where GGA-PBE [5] and the PAW pseudopotential [6] were used. The energy cutoff was set to 500 eV and the spin-orbit coupling effect was included. The crystal structures of *d*Lieb-MS_2 monolayers were fully optimized with the convergence criteria of 10^{-5} eV for energy and 0.01 eV/Å for force. The method of Methfessel-Paxton first-order spreading with the smearing width of 0.10 eV was employed to determine the occupancies of electrons in metallic bands. A uniform 30×30×1 Monkhorst-Pack **k**-point sampled in Brillouin zone was used to perform the structural relaxation and self-consistent calculations. The self-consistent calculations enable us to obtain the density-of-states (DOS) and spin-textures patterns, which were followed by non-self-consistent calculations to calculate the electronic band structures along high-symmetry directions.

The thermodynamic stability of screened *d*Lieb-MS_2 monolayer at finite-temperature has been checked by performing *ab initio* molecular dynamics simulations (AIMD) [8] based on the VASP [7], which lasted 5000 fs with the time step of 1 fs under the NVT ensemble. The AIMDs were simulated at the temperatures of 50, 100, 150, 200, 250, and 300 K, which were controlled by the Nose-Hoover thermostat. We only show the simulated results of maximum temperature at which the screened *d*Lieb-MS_2 monolayer can be stabilized. To make a reliable comparation with other transition metal dichalcogenides (TMDCs), the total energies of screened *d*Lieb-MS_2 (M=Zr, Nb, Mn, Fe, Re, Os) monolayers and related TMDCs monolayers (1T-ZrS_2, 1T-MnS_2, 1T-NbS_2, 1H-NbS_2, d1T″-ReS_2, 1T-MoS_2, 1H-MoS_2, 1T-WS_2, 1H-WS_2, and OsS_2 formed by pentagonal rings) were calculated by using VASP [7] under the **k**-points sampling with the uniform resolution of 0.04×2π $Å^{-1}$ in Brillouin zone.

Table S1. The elastic constants C_{ij} of *d*Lieb-MS_2 monolayers.

	C_{11} (N/m)	C_{12} (N/m)	C_{66} (N/m)
*d*Lieb-ZrS_2	31.8	2.3	2.7
*d*Lieb-NbS_2	25.3	11.0	6.6
*d*Lieb-MnS_2	32.6	4.1	9.0
*d*Lieb-FeS_2	38.8	15.1	6.2
*d*Lieb-ReS_2	33.4	9.7	9.5
*d*Lieb-OsS_2	38.4	16.1	4.1

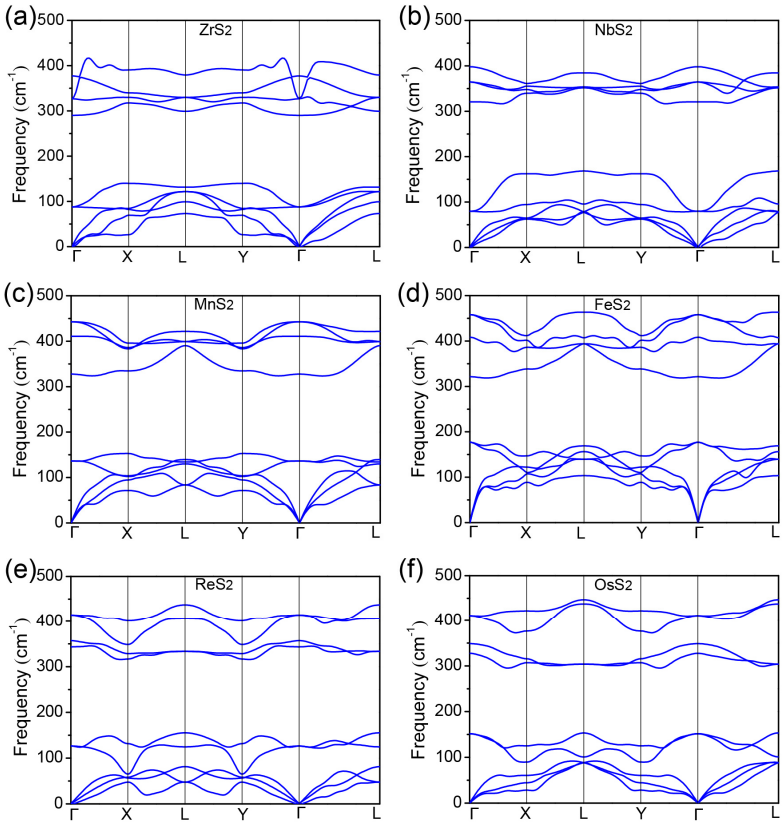

Figure S1. The phonon spectra of (a) *d*Lieb-ZrS_2, (b) *d*Lieb-NbS_2, (c) *d*Lieb-MnS_2, (d) *d*Lieb-FeS_2, (e) *d*Lieb-ReS_2, and (f) *d*Lieb-OsS_2.

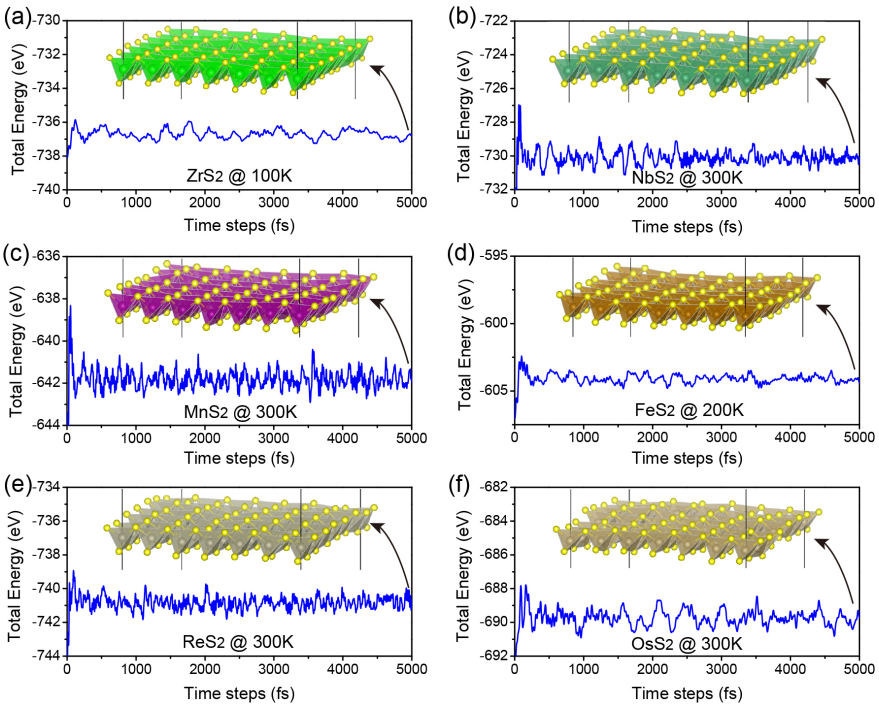

Figure S2. The variations of total energy during the AIMDs for the (a) *d*Lieb-ZrS_2 at 100 K, (b) *d*Lieb-NbS_2 at 300 K, (c) *d*Lieb-MnS_2 at 300 K, (d) *d*Lieb-FeS_2 at 200 K, (e) *d*Lieb-ReS_2 at 300 K, and (f) *d*Lieb-OsS_2 at 300 K. The insets are the crystal structures after simulating 5000 fs.

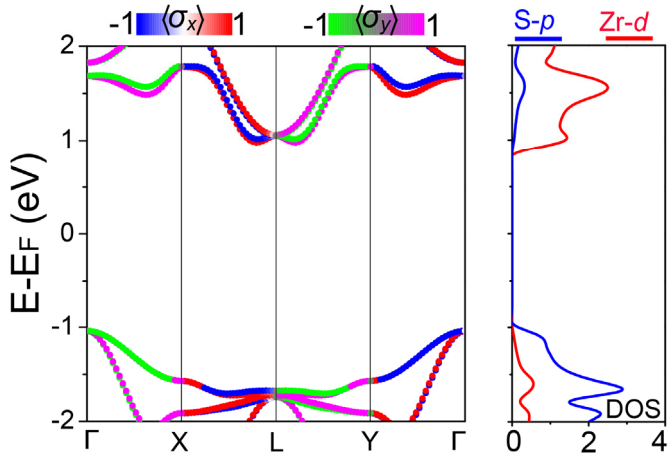

Figure S3. The band structure (left panel) and projected DOS (right panel) of *d*Lieb-ZrS_2. The colours on the band lines along the Γ-X and L-Y paths represent the expectation values $\langle\sigma_y\rangle$, while that along the X-L and Y-Γ paths represent the expectation values $\langle\sigma_x\rangle$. The projected DOS of Zr-*d* and S-*p* orbitals was plotted by using red and blue coloured lines, respectively.

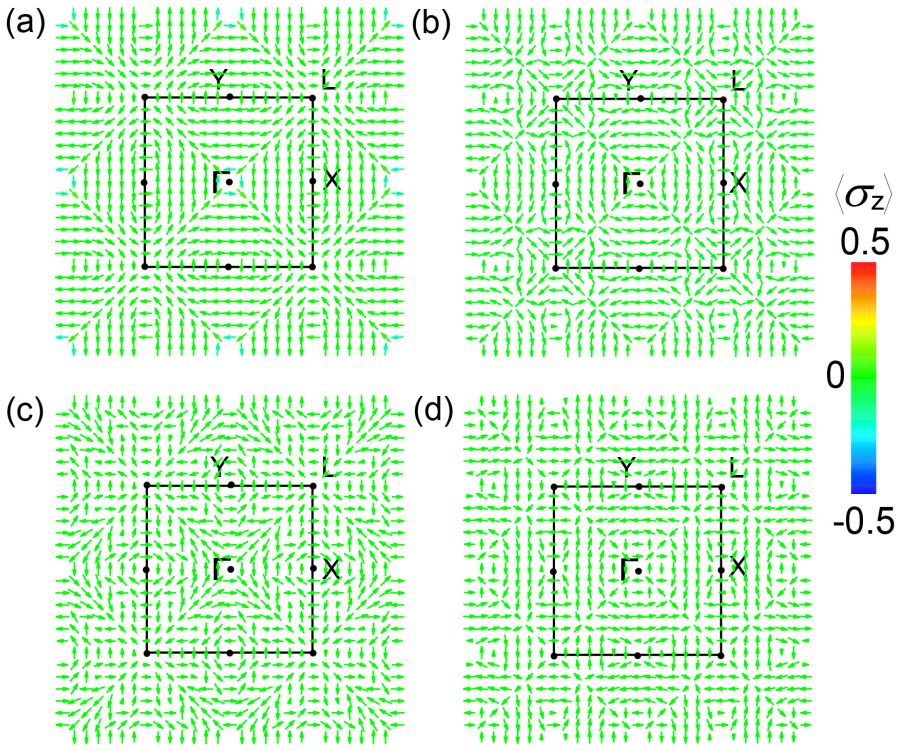

Figure S4. The spin texture patterns for the lowest band crossing the Fermi level of (a) *d*Lieb-NbS_2, (b) *d*Lieb-FeS_2, (c) *d*Lieb-ReS_2, and (d) *d*Lieb-OsS_2. The in-plane spin components are presented by arrows, while the colour represents out-of-plane component of spin orientation.

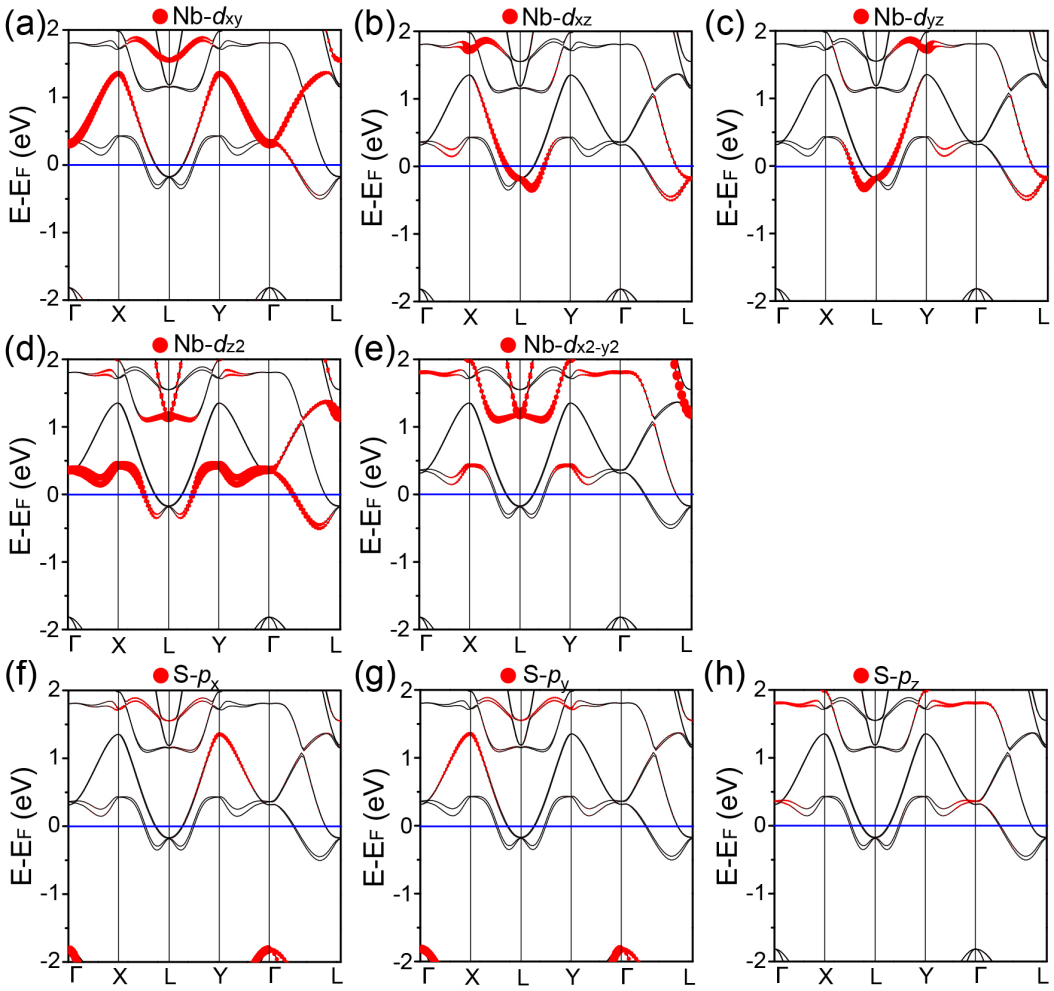

Figure S5. The orbital resolved band structures of *d*Lieb-NbS_2 with the contribution of (a) Nb-d_{xy}, (b) Nb-d_{xz}, (c) Nb-d_{yz}, (d) Nb-d_{z2}, (e) Nb-d_{x2-y2}, (f) S-p_x, (g) S-p_y, and (h) S-p_z orbital being drawn proportionally to the magnitude of red dots. The Fermi energy is set to zero.

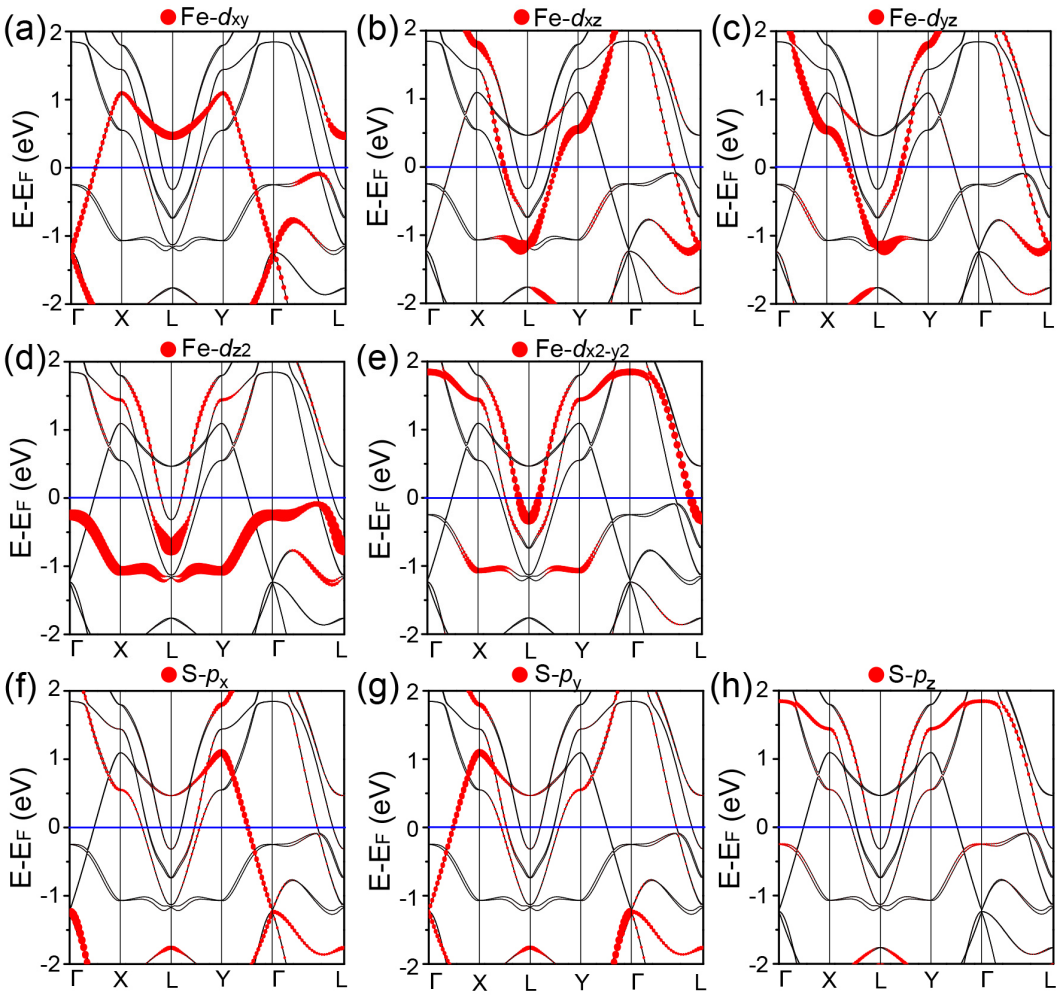

Figure S6. The orbital resolved band structures of *d*Lieb-FeS_2 with the contribution of (a) Fe-d_{xy}, (b) Fe-d_{xz}, (c) Fe-d_{yz}, (d) Fe-d_{z2}, (e) Fe-d_{x2-y2}, (f) S-p_x, (g) S-p_y, and (h) S-p_z orbital being drawn proportionally to the magnitude of red dots. The Fermi energy is set to zero.

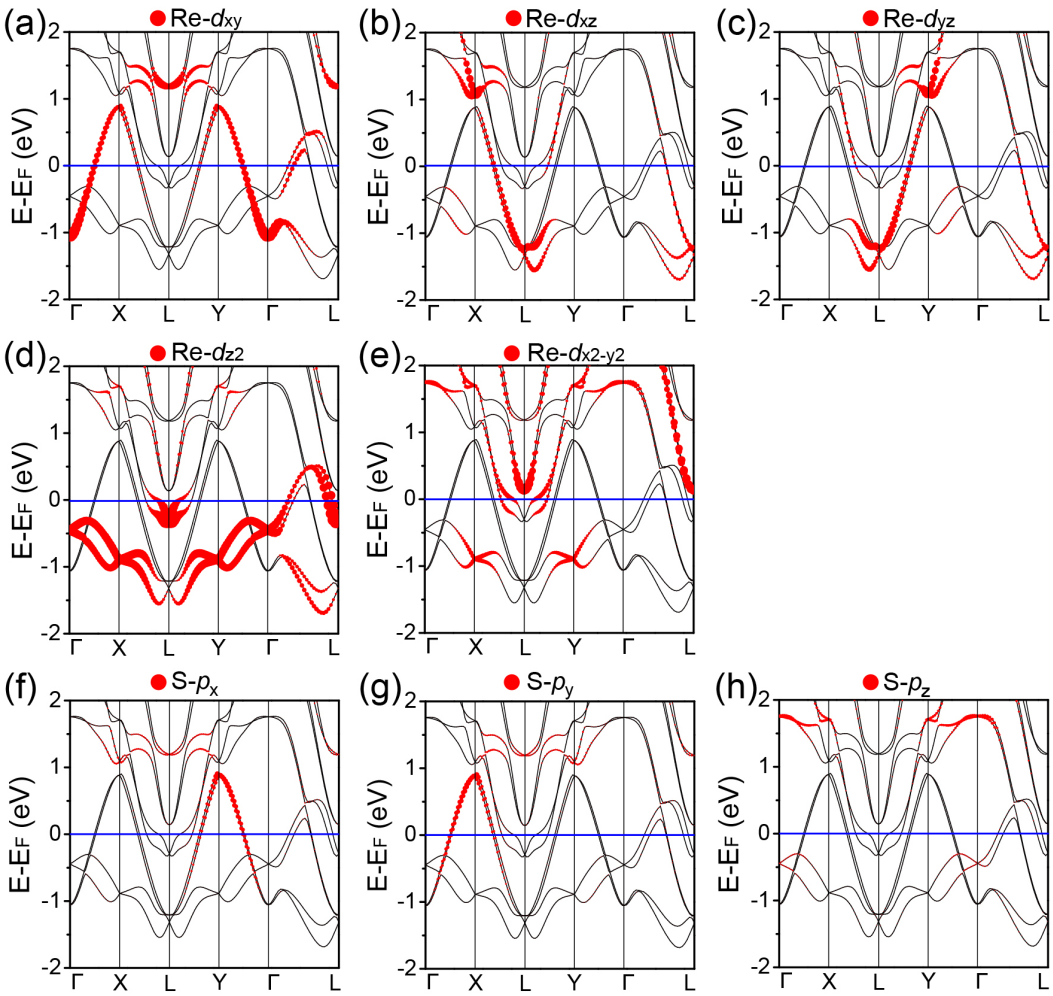

Figure S7. The orbital resolved band structures of *d*Lieb-ReS_2 with the contribution of (a) Re-d_{xy}, (b) Re-d_{xz}, (c) Re-d_{yz}, (d) Re-d_{z2}, (e) Re-d_{x2-y2}, (f) S-p_x, (g) S-p_y, and (h) S-p_z orbital being drawn proportionally to the magnitude of red dots. The Fermi energy is set to zero.

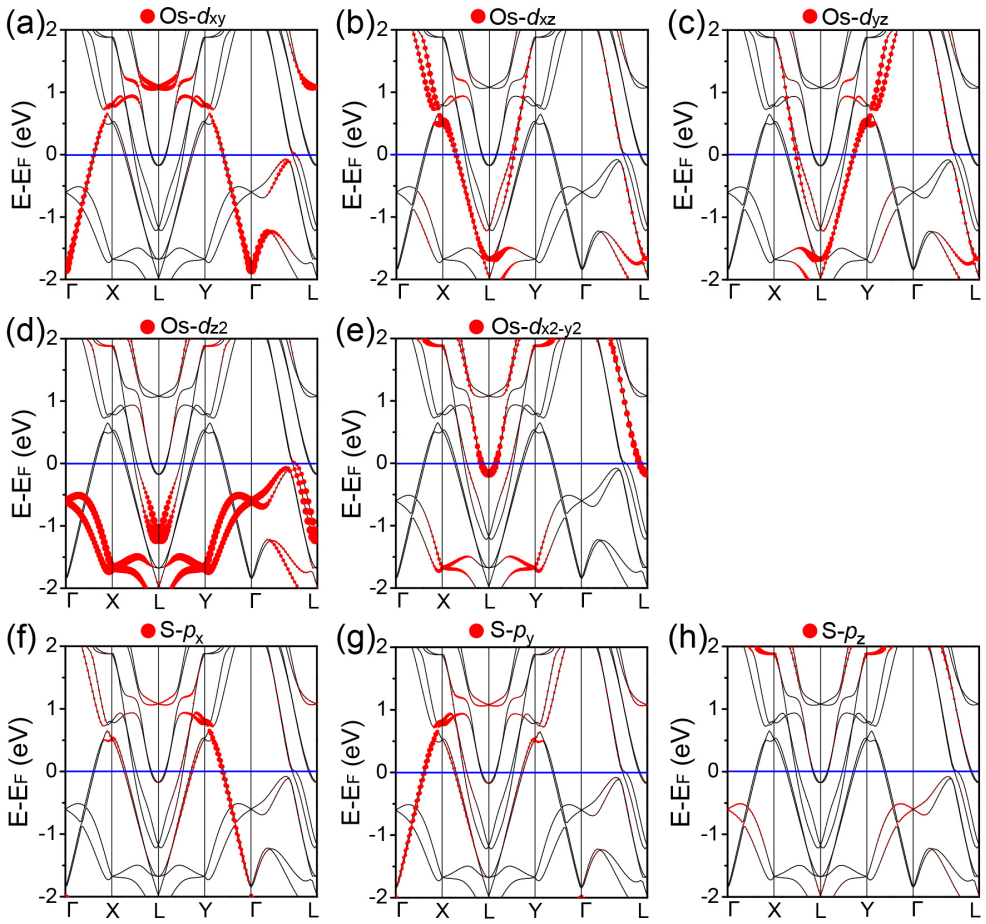

Figure S8. The orbital resolved band structures of *d*Lieb-OsS_2 with the contribution of (a) Os-d_{xy}, (b) Os-d_{xz}, (c) Os-d_{yz}, (d) Os-d_{z2}, (e) Os-d_{x2-y2}, (f) S-p_x, (g) S-p_y, and (h) S-p_z orbital being drawn proportionally to the magnitude of red dots. The Fermi energy is set to zero.

Section 2. The magnetic property of *d*Lieb-MnS_2 monolayer

To study the magnetic properties of the screened *d*Lieb-MS_2 (M=Zr, Nb, Mn, Fe, Re, Os) monolayers, we carry out spin-polarized calculations by assuming an initial non-zero magnetic moment on M atoms. The method of Methfessel-Paxton first-order spreading was employed to determine the occupancies of electrons in metallic bands. We have carefully checked the convergence of magnetic property by using different width of the smearing under a serious of **k**-points sampling in Brillouin zone. Our calculations indicate only the *d*Lieb-MnS_2 is magnetic, which is well converged when the **k**-points sampling exceeding 30×30×1 and the magnetic moment converged around ~0.8 μ_B per MnS_2 unit (Fig. S9). The existence of magnetism in *d*Lieb-MnS_2 and the absence of magnetism in *d*Lieb-NbS_2, *d*Lieb-FeS_2, and *d*Lieb-ReS_2 are also mentioned in the Computational 2D Materials Database [9]. Since the width of the smearing have little influence on the magnetic propriety when the **k**-points sampling exceeding 30×30×1 (Fig. S9), the smearing width of 0.10 eV is employed as an example to perform following calculations on the magnetic *d*Lieb-MnS_2 monolayer.

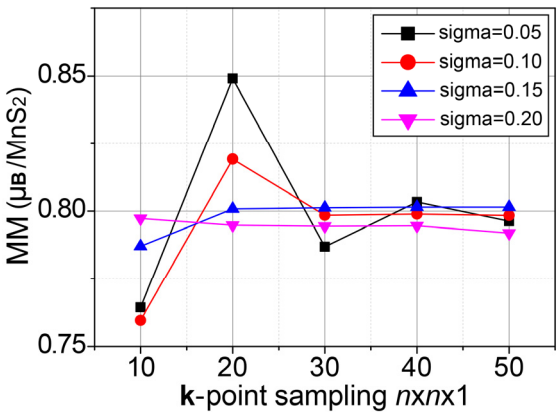

Figure S9. The dependence of magnetic moment (MM) per MnS_2 unit on the **k**-points sampling $n\times n\times 1$ and on the width (sigma=0.05, 0.10, 0.15, 0.20 eV) of smearing.

The magnetic ground state of *d*Lieb-MnS_2 was determined by total energy calculations, and the calculated total energy of magnetic *d*Lieb-MnS_2 monolayer is 5.2 meV/atom lower than that of *d*Lieb-MnS_2 without considering magnetism. The electronic band structure (Fig. S10a) and DOS (Fig. S10b) indicate the *d*Lieb-MnS_2 is a magnetic metal, because of both the up-spin and down-spin polarized electronic states crossing with the Fermi level. The iso-surface of the spin density for the magnetic *d*Lieb-MnS_2 (Fig. S10c) shows that the Mn atoms are highly spin-polarized and contribute mainly to the non-zero magnetic moment. The band structure of *d*Lieb-MnS_2 monolayer with considering spin-orbit coupling was plotted in Fig. S10d, which is qualitatively consistent with that calculated without spin-orbit coupling (Fig. S10a).

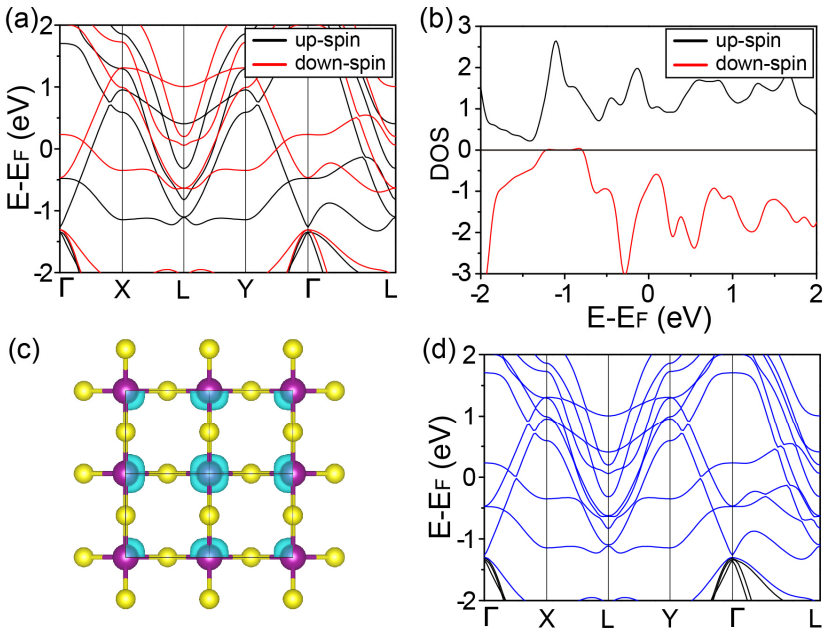

Figure S10. (a, b) The electronic band structure (a) and DOS (b) of magnetic *d*Lieb-MnS_2 monolayer. The up-spin and down-spin components are respectively plotted by using black and red lines. (c) The real-space distribution of spin density. (d) The band structure of magnetic *d*Lieb-MnS_2 monolayer with considering spin-orbit coupling.

To reveal the origin of the magnetism in *d*Lieb-MnS_2 monolayer, we compare the total DOS of *d*Lieb-MnS_2 without considering magnetism to that of nonmagnetic *d*Lieb-MS_2 (M= Nb, Fe, Re, Os) monolayers in Fig. S11a. One can clearly see the *d*Lieb-MnS_2 possesses the largest DOS at the Fermi level, which is related to the band lines of localized $3d_{z^2}$-orbitals crossing with the Fermi level (Fig. S11b). The largest DOS of *d*Lieb-MnS_2 at the Fermi level can be greatly reduced by introducing magnetism (inset of Fig. S11a). Together with the odd number of electrons per Mn atom, the emergence of magnetism in *d*Lieb-MnS_2 can be attributed to the Stoner effect [10, 11], and a large DOS of localized *d*-orbitals at the Fermi level tends to inducing magnetic instability. This can be demonstrated by analyzing the magnetic property of *d*Lieb-MnS_2 under different biaxial compressive strain. The total DOS of *d*Lieb-MnS_2 without considering magnetism is basically unchanged when the magnitude of compressive strain is smaller than 2% and decreases when increasing the magnitude of compressive strain from 2% (Fig. S11c). Then the calculations with considering spin polarization were performed on the compressed *d*Lieb-MnS_2 to evaluate the magnetic moment (Fig. S11d), which show that the magnetism can be well maintained when the magnitude of compressive strain is smaller than 2%, and will transform to non-magnetic state when further increasing the magnitude of compressive strain from 2%. The closely correlation between the magnetism and the magnitude of DOS at the Fermi level indeed reveals that the Stoner effect plays important role.

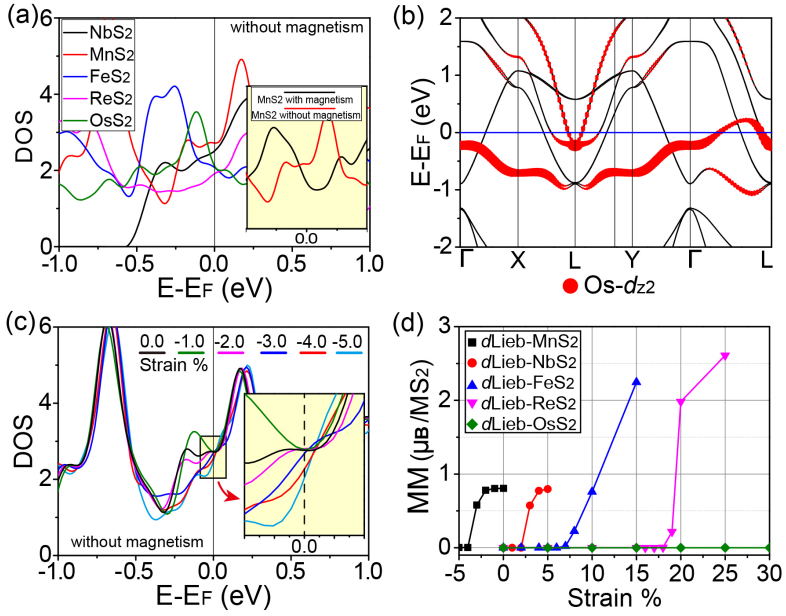

Figure S11. (a) The comparation between the total DOS of *d*Lieb-MnS_2 without considering magnetism and that of nonmagnetic *d*Lieb-MS_2 (M= Nb, Fe, Re, Os) monolayers. Inset plots the comparation between the total DOS of *d*Lieb-MnS_2 with and without considering magnetism. (b) The band structures of *d*Lieb-MnS_2 without considering magnetism, where the contribution of Mn-d_{z^2} is drawn proportionally to the magnitude of red dots. (c) The variation of the total DOS of *d*Lieb-MnS_2 without considering magnetism under different biaxial compressive strain. (d) The magnetic moment (MM) per MS_2 unit under different biaxial strain for the *d*Lieb-MS_2.

To further confirm above analysis, we propose the Stoner magnetism can be induced and controlled in other metallic *d*Lieb-MS_2 monolayers by applying biaxial tensile strains (Fig. S11d), which plays the role of making the *d*-orbitals of M atom more localized and thus induce the magnetic instability. Specifically, one can see the magnetic moment of *d*Lieb-NbS_2 at the tensile strain of 5% is nearly equal to that of equilibrium *d*Lieb-MnS_2. This fact can be understood from that the Nb atoms possesses odd number of electrons and the localized $4d_{z^2}$-orbitals also form narrow band lines crossing with Fermi level (Fig. S5). For the *d*Lieb-ReS_2 with odd number of electrons, a larger tensile strain is demanded to introducing the magnetism due to the $5d_{z^2}$-orbitals of Re atoms are less localized, which can be seen from the its band structures (Fig. S7). For the *d*Lieb-FeS_2 and *d*Lieb-OsS_2 with even number of electrons, the band lines of d_{z^2}-orbitals no longer cross with the Fermi level (Fig. S6 and S8). Despite this, the tensile strain could also introduce the Stoner magnetism in *d*Lieb-FeS_2 due to the localized 3*d*-orbitals, while the less localized 5*d*-orbitals of Os still preserve the time-reversal symmetry of *d*Lieb-OsS_2 even if the tensile strain reach up to 30% (Fig. S11d). Furthermore, the dependence of magnetic property on the tensile strain also demonstrate that the *d*Lieb-MS_2 (M=Nb, Fe, Re, Os) monolayers are indeed nonmagnetic metals at their equilibrium crystal structures (Fig. S11d), which is compatible with the existence of superconductivity.

Section 3. Details of estimating the superconductivity of *d*Lieb-MS_2 monolayer

During the calculations of phonon spectra within the framework of DFPT [4], the electron-phonon coupling (EPC) strength was estimated for the metallic *d*Lieb-MS_2 (M=Nb, Re, Fe, Os) monolayer by using the QE package [1] based on the DFT [2, 3]. The dynamic matrix and phonon frequency of optimized *d*Lieb-MS_2 were computed on a 10×10×1 **q**-point mesh with a 20×20×1 **k**-point sampling, and a finer 40×40×1 **k**-point grid is used in the EPC calculations. Specifically, the EPC was calculated via $\lambda(\omega) = 2\int_0^{\omega} d\omega' \frac{\alpha^2F(\omega')}{\omega'}$ [12], where the Eliashberg spectral function $\alpha^2F(\omega)$ is defined by $\alpha^2F(\omega) = \frac{1}{2}\sum_{\mathbf{q}v} w_{\mathbf{q}}\omega_{\mathbf{q}v}\lambda_{\mathbf{q}v}\delta(\omega - \omega_{\mathbf{q}v})$. The momentum **q** and mode *v* resolved EPC $\lambda_{\mathbf{q}v}$ is given by $\lambda_{\mathbf{q}v} = \frac{\hbar}{2m_0N_F\omega_{\mathbf{q}v}^2}\sum_{mn\mathbf{k}} w_{\mathbf{k}} \left|\langle\psi_{m\mathbf{k}+\mathbf{q}}|\partial_{\mathbf{q}v}V|\psi_{n\mathbf{k}}\rangle\right|^2 \delta(\epsilon_{n\mathbf{k}})\delta(\epsilon_{m\mathbf{k}+\mathbf{q}})$ and shown in Fig. S12. The $\psi_{n\mathbf{k}}$ is the electronic wavefunction for band *n*, wavevector **k**, and eigenvalue $\epsilon_{n\mathbf{k}}$. $\partial_{\mathbf{q}v}V$ is the derivative of self-consistent potential associated with the phonon wavevector **q**, phonon branch v and phonon frequency $\omega_{\mathbf{q}v}$. δ is the Dirac delta function. The $w_{\mathbf{k}}$ and $w_{\mathbf{q}}$ are respectively the Brillouin zone weight of **k**-point and **q**-point. m_0 is the convenient reference mass and N_F is DOS at the Fermi level. The total EPC λ corresponds to the value of $\lambda(\omega_{max})$ with the ω_{max} being the maximum of phonon frequency.

We employ the Allen-Dynes-modified McMillan equation [13, 14] to evaluate the superconducting transition temperatures T_C with the Coulomb pseudopotential $\mu^* = 0.1$. For the *d*Lieb-MS_2 with the total EPC $\lambda < 1.5$, the Allen-Dynes-modified McMillan equation without correction factors was employed, which is given by

$$T_C = \frac{\omega_{\log}}{1.2} \exp\left[\frac{-1.04 \times (1+\lambda)}{\lambda - \mu^* \times (1 + 0.62 \times \lambda)}\right]$$

where the logarithmically averaged frequency ω_{log} is defined by $\omega_{log} = exp\left[\frac{2}{\lambda}\int \frac{\alpha^2 F(\omega)}{\omega} log(\omega) d\omega\right]$. This equation is the most widely used approach for the calculation of T_C from first principles [15]. For the *d*Lieb-MS_2 with the total EPC $\lambda > 1.5$, the correction factors f_1 and f_2 were included in the Allen-Dynes-modified McMillan equation:

$$T_C = \frac{f_1 f_2 \omega_{\log}}{1.2} \exp\left[\frac{-1.04 \times (1+\lambda)}{\lambda - \mu^* \times (1 + 0.62 \times \lambda)}\right]$$

with $f_1 = \sqrt[3]{\left[1 + \left(\frac{\lambda}{2.46(1+3.8\mu^*)}\right)^{\frac{3}{2}}\right]}$, $f_2 = 1 + \frac{\left(\frac{\bar{\omega}_2}{\omega_{\log}} - 1\right)\lambda^2}{\lambda^2 + \left[1.82(1+6.3\mu^*)\frac{\bar{\omega}_2}{\omega_{\log}}\right]^2}$. Here the mean square frequency $\bar{\omega}_2$ is defined by $\bar{\omega}_2 = \sqrt{\frac{2}{\lambda}\int_0^\infty \alpha^2 F(\omega)\omega d\omega}$. This extended form of Allen-Dynes-modified McMillan equation is so accurate that the predicted T_C is usually identical to those obtained by the solution of the Eliashberg equations for conventional superconductors [15].

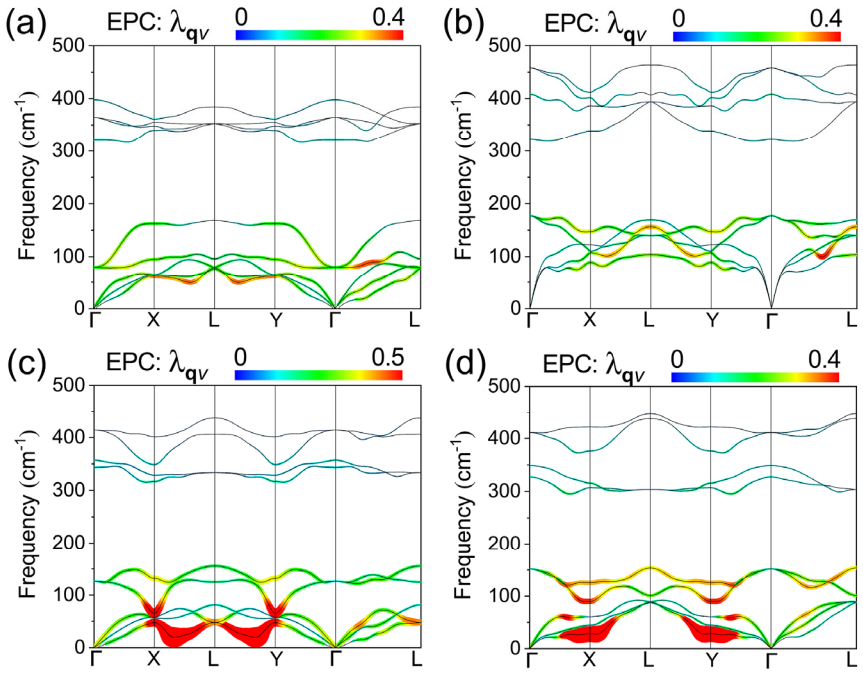

Figure S12. The phonon spectra of (a) *d*Lieb-NbS_2, (b) *d*Lieb-FeS_2, (c) *d*Lieb-ReS_2, and (d) *d*Lieb-OsS_2, where the coloured dots are drawn proportionally to the magnitude of momentum **q** and mode *v* resolved EPC $\lambda_{\mathbf{q}v}$.

Section 4. The feasibility of exfoliating *d*Lieb-MS_2 monolayer

We here propose the *d*Lieb-MS_2 monolayer can be exfoliated from its bulk counterpart, based on first-principles calculating the formation energy E_{form} of bulk *d*Lieb-MS_2 and the exfoliation energy E_{XF} of *d*Lieb-MS_2 monolayer from *d*Lieb-MS_2 slab. The first-principles calculations were performed by including van der Waals interaction, which is described by DFT-D3 functional with Becke-Jonson damping and implemented in the VASP [7]. The GGA-PBE [5] was employed for the PAW pseudopotential [6] and the energy cutoff was set to 500 eV. The **k**-points with the resolution of $0.04\times2\pi$ Å^{-1} were sampled in Brillouin zone. The crystal structures of bulk *d*Lieb-MS_2 and related materials were fully optimized with the convergence criteria of 10^{-5} eV for energy and 0.01 eV/Å for force. The total energy was calculated by self-consistent calculations, which were followed by non-self-consistent calculations to calculate the electronic band structures along high-symmetry directions.

Firstly, the total energy was employed to determine the most favorable stacking patterns of bulk *d*Lieb-MS_2. Referring to the symmetry of *d*Lieb-MS_2 monolayer, there are eight stacking patterns can be constructed, including AA (Fig. S13a), AB[$X_{0.5}$] (Fig. S13b), AB[$Y_{0.5}$] (Fig. S13c), AB[$X_{0.5}|Y_{0.5}$] (Fig. S13d), AB[R_{90}] (Fig. S13e), AB[$X_{0.5}|R_{90}$] (Fig. S13f), AB[$Y_{0.5}|R_{90}$] (Fig. S13g), AB[$X_{0.5}|Y_{0.5}|R_{90}$] (Fig. S13h) stacking. Here the [$X_{0.5}$] and [$Y_{0.5}$] mean the layer B moving half lattice constant with respect to the layer A along X and Y direction, respectively. The [R_{90}] means the layer B rotating by 90°. The combination between the [$X_{0.5}$], [$Y_{0.5}$], and [R_{90}] means these operations are performed sequentially. The calculated total energy (Table S2) of bulk *d*Lieb-MS_2 with different stacking patterns indicates all of the *d*Lieb-MS_2 favorite the AB[$X_{0.5}|Y_{0.5}|R_{90}$] stacking with the space group of $P4_2/nmc$, except the AA stacked *d*Lieb-FeS_2 with the space group of $P\bar{4}m2$ possessing low total energy. Consequently, the following calculations were conducted on the AB[$X_{0.5}|Y_{0.5}|R_{90}$] stacked *d*Lieb-ZrS_2, *d*Lieb-NbS_2, *d*Lieb-MnS_2, *d*Lieb-ReS_2, and *d*Lieb-OsS_2, as well as the AA stacked *d*Lieb-FeS_2.

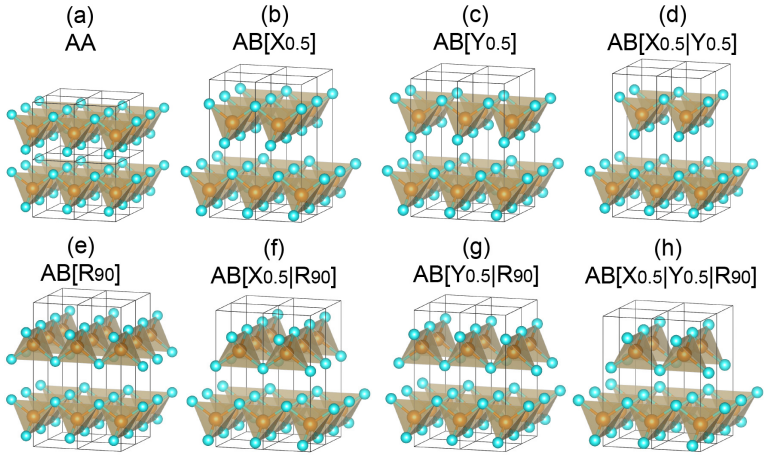

Figure S13. The crystal structures of bulk *d*Lieb-MS_2 constructed by (a) AA, (b) AB[$X_{0.5}$], (c) AB[$Y_{0.5}$], (d) AB[$X_{0.5}|Y_{0.5}$], (e) AB[R_{90}], (f) AB[$X_{0.5}|R_{90}$], (g) AB[$Y_{0.5}|R_{90}$], and (h) AB[$X_{0.5}|Y_{0.5}|R_{90}$] stacking.

Table S2. The energy difference between the ground state pattern and other stacking patterns of bulk *d*Lieb-MS_2. The total energy of ground state pattern is set to 0.00 eV, and the unit of the energy difference is meV/atom.

	***d*Lieb-ZrS_2**	***d*Lieb-NbS_2**	***d*Lieb-MnS_2**	***d*Lieb-FeS_2**	***d*Lieb-ReS_2**	***d*Lieb-OsS_2**
AA	1.94	3.96	0.54	0.00	8.05	5.72
AB[$X_{0.5}$]	24.94	23.48	38.88	21.96	36.55	36.73
AB[$Y_{0.5}$]	24.94	23.48	38.88	21.96	36.55	36.73
AB[$X_{0.5}$|$Y_{0.5}$]	39.39	37.97	73.44	41.01	62.40	67.78
AB[R_{90}]	42.15	40.01	89.66	68.26	67.21	76.87
AB[$X_{0.5}$|R_{90}]	26.12	23.18	47.25	20.78	40.96	39.70
AB[$Y_{0.5}$|R_{90}]	26.12	23.18	47.25	20.78	40.96	39.70
AB[$X_{0.5}$|$Y_{0.5}$|R_{90}]	0.00	0.00	0.00	4.33	0.00	0.00

Next, the formation energy E_{form} of bulk *d*Lieb-MS_2 was calculated to demonstrate their experimental feasibility. The E_{form} is defined as $E_{\mathrm{form}} = (E_{\mathrm{total}} - \mu_{\mathrm{M}} - 2E_{\mathrm{S}})/3$, where the E_{total} is the total energy of bulk *d*Lieb-MS_2 per MS_2 unit and the E_{S} is the energy of *S* atom in bulk S_6. The energy of M atom μ_{M} is evaluated by $\mu_{\mathrm{M}} = E_{\mathrm{M}}/2$, where E_{M} is the total energy per primitive cell of body-center-cubic bulk M (M=Nb, Mn, and Fe) or of hexagonal bulk M (M=Zr, Re, and Os). To verify the correctness of our calculation, we calculated the formation energy of 2H-MoS_2 to be 2.85 eV per MoS_2 unit, which is in agreement with the previously reported 2.88 eV [16]. We also calculated the formation energy of 1T-MoS_2, 2H-WS_2, and 1T-WS_2 for comparation, where the μ_{M} is evaluated by $\mu_{\mathrm{M}} = E_{\mathrm{M}}/2$ and E_{M} is the total energy per primitive cell of body-center-cubic bulk M (M=Mo and W). The calculated formation energies for different TMDCs were summarized in Fig. S14. One can clearly see the formation energies are all negative except *d*Lieb-OsS_2, indicating the feasibility of preparing the bulk *d*Lieb-MS_2 (M=Zr, Nb, Mn, Fe, and Re) in experiments. Since the OsS_2 monolayer constructed by pentagonal rings [17] is 0.19 eV/atom higher than the energy of *d*Lieb-OsS_2 monolayer with dynamic, mechanical, and thermodynamic stability, we hope the bulk *d*Lieb-OsS_2 with extremely small positive E_{form} to be exist because of its thermodynamic stability at room temperature (Fig. 15f). Even through the E_{form} of *d*Lieb-ZrS_2 (Fig. S14a), *d*Lieb-NbS_2 (Fig. S14b), *d*Lieb-ReS_2 (Fig. S14e) is respectively higher than that of the synthesized 1T- ZrS_2, 1T-NbS_2, d1T''-ReS_2, the energy difference is comparable to that between the synthesized 1T- and 2H-MoS_2 (Fig. S14g) or that between the synthesized 1T- and 2H-WS_2 (Fig. S14h). We thus expect the *d*Lieb-MS_2 to be experimentally synthesized under special condition.

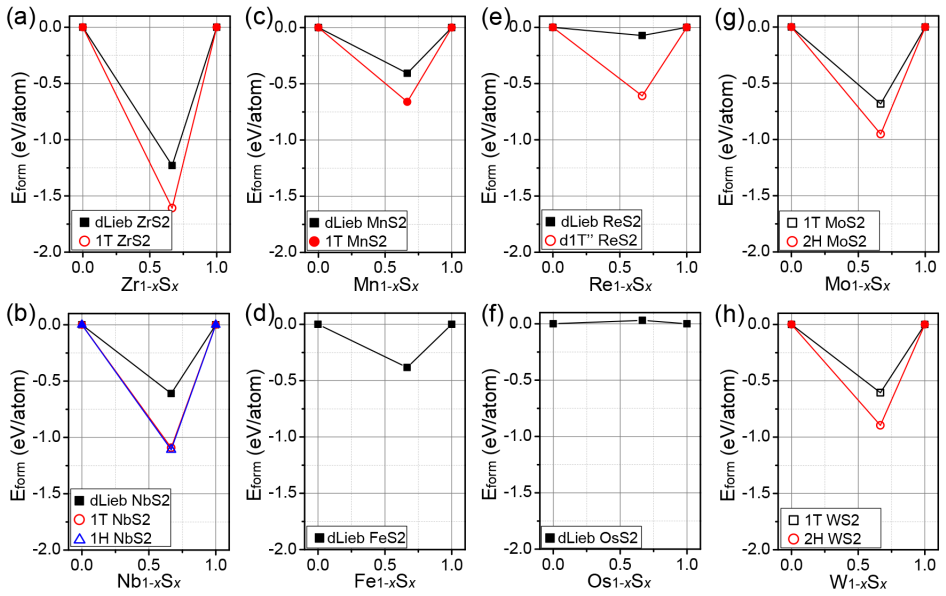

Figure S14. The convex hull of formation energy for the bulk *d*Lieb-MS_2 and related TMDCs. The opened symbols mean the corresponding TMDC was experimentally synthesized.

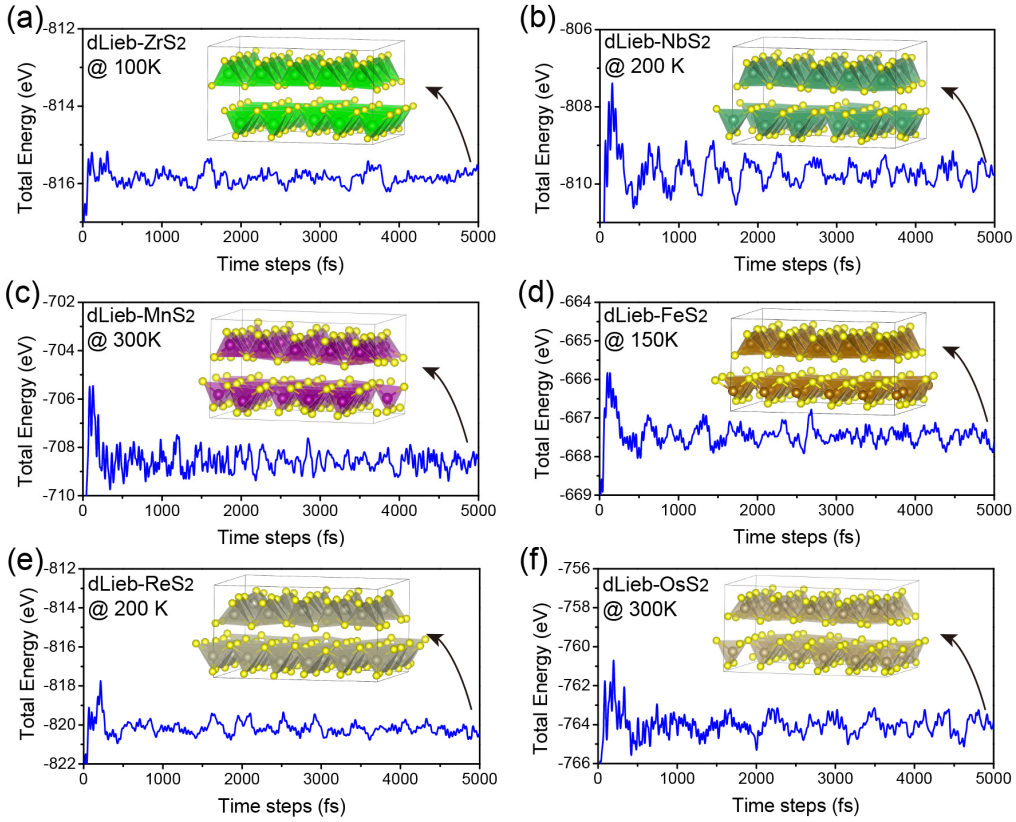

Figure S15. The variations of the total energy during the AIMDs for the (a) bulk *d*Lieb-ZrS_2 at 100 K, (b) bulk *d*Lieb-NbS_2 at 200 K, (c) bulk *d*Lieb-MnS_2 at 300 K, (d) bulk *d*Lieb-FeS_2 at 150 K, (e) bulk *d*Lieb-ReS_2 at 200 K, and (f) bulk *d*Lieb-OsS_2 at 300 K. The insets are the crystal structures after simulating 5000 fs.

The thermodynamic stability of bulk *d*Lieb-MS_2 at finite-temperature has been checked by AIMD [8], which ran for 5000 fs with the time step of 1 fs under the NVT ensemble and was implemented in the VASP [7]. The AIMDs were simulated at the temperatures of 50, 100, 150, 200, 250, and 300 K, which were controlled by the Nose-Hoover thermostat. We only show the simulated results (Fig. S15) of maximum temperature at which the bulk *d*Lieb-MS_2 can be stabilized. One can clearly see simulated total energy converges well and the crystal structures are well maintained for the *d*Lieb-ZrS_2 at 100 K (Fig. S15a), the *d*Lieb-NbS_2 at 200 K (Fig. S15b), the *d*Lieb-MnS_2 at 300 K (Fig. S15c), the *d*Lieb-FeS_2 at 150 K (Fig. S15d), the *d*Lieb-ReS_2 at 200 K (Fig. S15e), and the *d*Lieb-OsS_2 at 300 K (Fig. S15f), indicating their thermodynamic stability. It should mention that the lower stabilized temperatures of bulk *d*Lieb-NbS_2, bulk *d*Lieb-FeS_2, and bulk *d*Lieb-ReS_2 than that of their monolayer counterparts (Fig. S2) can be attributed to the interlayer interactions in bulk *d*Lieb-MS_2.

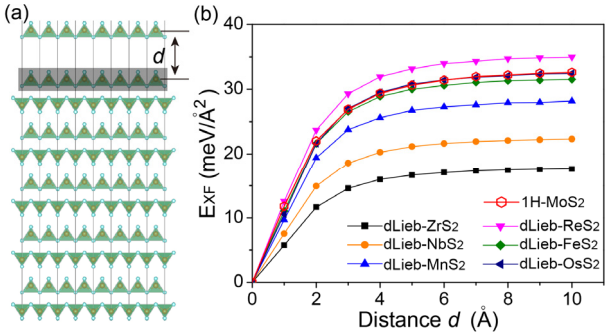

Figure S16. (a) The crystal structure of *d*Lieb-MS_2 slab used to calculating exfoliation energy E_{XF}, where the topmost monolayer is separated from the rest by the distance of *d*. (b) The calculated exfoliation energy of *d*Lieb-MS_2 monolayer compared with that of 1H-MoS_2 monolayer.

Then, we calculated the exfoliation energy E_{XF} to evaluate the cost of removing a single layer from the surface of the bulk compound, which is defined as $E_{XF} = (E_{n-1} + E_1 - E_n)/A$. Here A is the area of the *d*Lieb-MS_2 slab. E_n is the total energy of *d*Lieb-MS_2 slab consisting of n layers of *d*Lieb-MS_2, and the $E_{n-1} + E_1$ is total energy of the *d*Lieb-MS_2 slab with one *d*Lieb-MS_2 layer being separated from the rest (n-1) layers (Fig. S16a). The correctness of our calculation was verified by calculating the E_{XF} of 1H-MoS_2 monolayer to be 32.59 meV/Å^2, which is in agreement with the previously reported 30.82 meV/Å^2 [18]. Our calculated E_{XF} are smaller than that of 1H-MoS_2 monolayer for most *d*Lieb-MS_2 monolayer (Fig. S16b), which demonstrates the feasibility of exfoliating *d*Lieb-MS_2 monolayer from its bulk counterparts.

Lastly, we present the electronic band structures of the AB[$X_{0.5}|Y_{0.5}|R_{90}$] stacked *d*Lieb-MS_2 (Mn=Zr, Nb, Re, Os) and AA stacked *d*Lieb-FeS_2 in Fig. S17. One can see the stacking do not eliminate the band gap of *d*Lieb-ZrS_2 and do not destroy the metallicity of *d*Lieb-MS_2 (M= Nb, Fe, Re, Os). Because the space group of $P4_2/nmc$ is centrosymmetric, the band structures of AB[$X_{0.5}|Y_{0.5}|R_{90}$] stacked *d*Lieb-ZrS_2 (Fig. S17a), *d*Lieb-NbS_2 (Fig. S17b), *d*Lieb-ReS_2 (Fig. S17d), and *d*Lieb-OsS_2 (Fig. S17e) are at least doubly degenerated, while the degeneracy is removed in certain band lines

of AA stacked *d*Lieb-FeS_2 (Fig. S17c) with the non-centrosymmetric space group of $P\bar{4}m2$. The magnetic *d*Lieb-MnS_2 also tends to form the AB[$X_{0.5}$|$Y_{0.5}$|R_{90}] stacking, which is 0.54 meV/atom lower than that the AA stacked *d*Lieb-MnS_2 (Table S2). Considering the small energy difference, we respectively plot the band structures of AA and AB[$X_{0.5}$|$Y_{0.5}$|R_{90}] stacked *d*Lieb-MnS_2 in Fig. S18a-b and S18c-d. Clearly, the magnetic property of *d*Lieb-MnS_2 is well preserved for both stacking patterns, and the band structures without (Fig. S18a and S18c) and with (Fig. S18b and S18d) considering spin-orbit coupling are qualitatively consistent with each other.

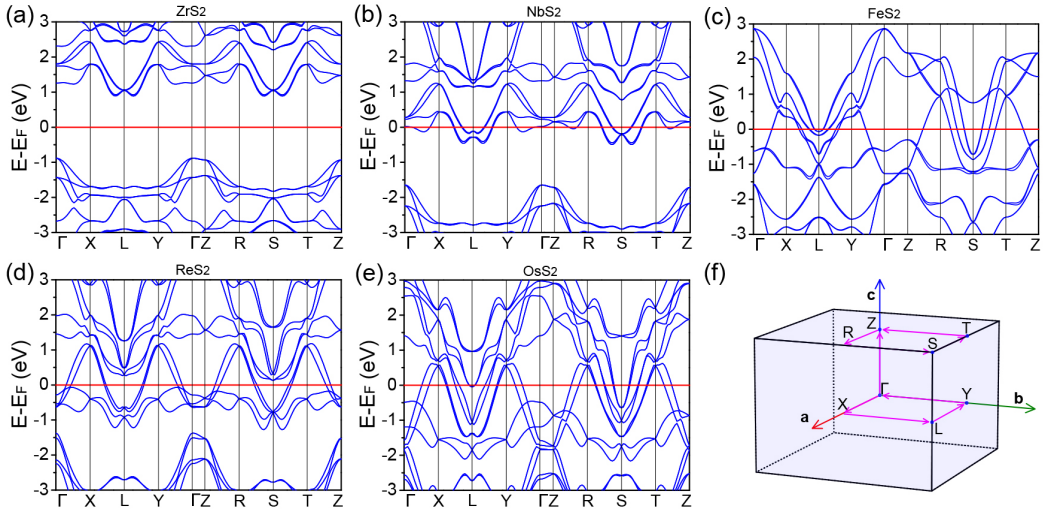

Figure S17. The electronic band structure of (a) AB[$X_{0.5}$|$Y_{0.5}$|R_{90}] stacked *d*Lieb-ZrS_2, (b) AB[$X_{0.5}$|$Y_{0.5}$|R_{90}] stacked *d*Lieb-NbS_2, (c) AA stacked *d*Lieb-FeS_2, (d) AB[$X_{0.5}$|$Y_{0.5}$|R_{90}] stacked *d*Lieb-ReS_2, (e) AB[$X_{0.5}$|$Y_{0.5}$|R_{90}] stacked *d*Lieb-OsS_2. (f) The Brillouin zone of bulk *d*Lieb-MS_2 and the **k**-point paths used to calculate electronic band structures.

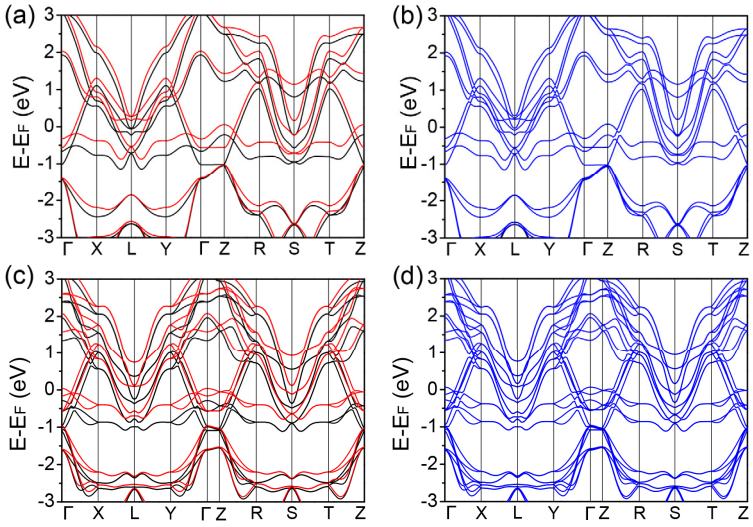

Figure S18. The electronic band structure of (a, b) AA stacked and (c, d) AB[$X_{0.5}$|$Y_{0.5}$|R_{90}] stacked *d*Lieb-MnS_2 (a, c) without and (b, d) with considering spin-orbit coupling.

References

1 P. Giannozzi, O. Baseggio, P. Bonfà, D. Brunato, R. Car, I. Carnimeo, C. Cavazzoni, S. de Gironcoli, P. Delugas, F. Ferrari Ruffino, A. Ferretti, N. Marzari, I. Timrov, A. Urru and S. Baroni, *J. Chem. Phys.*, 2020, **152**, 154105.

2 P. Hohenberg and W. Kohn, *Phys. Rev.*, 1964, **136**, B864-B871.

3 W. Kohn and L. J. Sham, *Phys. Rev.*, 1965, **140**, A1133-A1138.

4 S. Baroni, S. de Gironcoli, A. Dal Corso and P. Giannozzi, *Rev. Mod. Phys.*, 2001, **73**, 515-562.

5 J. P. Perdew, K. Burke and M. Ernzerhof, *Phys. Rev. Lett.*, 1996, **77**, 3865-3868.

6 P. E. Blöchl, *Phys. Rev. B*, 1994, **50**, 17953-17979.

7 G. Kresse and J. Furthmüller, *Comput. Mater. Sci.*, 1996, **6**, 15-50.

8 S. Nosé, *J. Chem. Phys.*, 1984, **81**, 511-519.

9 M. N. Gjerding, A. Taghizadeh, A. Rasmussen, S. Ali, F. Bertoldo, T. Deilmann, N. R. Knøsgaard, M. Kruse, A. H. Larsen, S. Manti, T. G. Pedersen, U. Petralanda, T. Skovhus, M. K. Svendsen, J. J. Mortensen, T. Olsen and K. S. Thygesen, *2D Mater.*, 2021, **8**, 044002.

10 W. Jiang, H. Huang and F. Liu, *Nat. Commun.*, 2019, **10**, 2207.

11 B. Cui, X. Zheng, J. Wang, D. Liu, S. Xie and B. Huang, *Nat. Commun.*, 2020, **11**, 66.

12 P. B. Allen, *Phys. Rev. B*, 1972, **6**, 2577-2579.

13 W. L. McMillan, *Phys. Rev.*, 1968, **167**, 331-344.

14 P. B. Allen and R. C. Dynes, *Phys. Rev. B*, 1975, **12**, 905-922.

15 J. A. Flores-Livas, L. Boeri, A. Sanna, G. Profeta, R. Arita and M. Eremets, *Phys. Rep.*, 2020, **856**, 1-78.

16 D. Liu, Y. Guo, L. Fang and J. Robertson, *Appl. Phys. Lett.*, 2013, **103**.

17 Z.-x. Pang, X.-K. Hu and P. Li, *Chem. Phys.*, 2021, **547**, 111199.

18 T. Björkman, A. Gulans, A. V. Krasheninnikov and R. M. Nieminen, *Phys. Rev. Lett.*, 2012, **108**, 235502.